




Flagellar elasticity and the multiple swimming modes of interfacial bacteriaS. Bianchi ¹, F. Saglimbeni,¹ G. Frangipane ^{2,3} and R. Di Leonardo ^{3,1,*}¹*Soft and Living Matter Laboratory, NANOTEC-CNR, Institute of Nanotechnology, Rome 00185, Italy*²*Center for Life Nano and Neuro Science, Italian Institute of Technology, Rome 00161, Italy*³*Department of Physics, “Sapienza” University of Rome, Rome 00185, Italy*

(Received 12 August 2021; revised 16 November 2021; accepted 6 May 2022; published 24 May 2022)

In peritrichous bacteria, such as *E. coli*, flagella join into a compact bundle that is usually assumed to be rigidly connected to the cell body allowing only counter-rotations around a common axis. This simple microswimmer model has been very successful in providing quantitative predictions on swimming behavior in bulk fluids and in the proximity of different kinds of interfaces and confinement. Here, we show that, when bacteria colonize a water-air interface, capillary forces can strongly deform the body-bundle complex, giving rise to unusual and heterogeneous swimming modes. We find that all trajectories can be classified into four main modes, with cells tracing either clockwise or counterclockwise circles while the cell body can be locked to the swimming direction or spin freely. All the observed phenomenology can be reproduced by simply allowing elastic bending of the bundle axis, where stiffness is the main factor in selecting the swimming mode. Our results allow us to experimentally test flexible models of microswimmers in highly perturbed contexts and provide physical insights into the early stages of bacterial pellicles.

DOI: [10.1103/PhysRevResearch.4.L022044](https://doi.org/10.1103/PhysRevResearch.4.L022044)

Bacteria can colonize air-water interfaces by forming pellicles [1]. Unlike biofilms over solid substrates, little is known about pellicles in general and even about the dynamics of individual cells that breach the interface [2]. This is not surprising if we consider that even for colloidal spheres, the static and dynamic properties at the interfaces can be nontrivial. For instance, contact lines reach equilibrium through slow hopping processes recalling aging in glassy systems [3]. Contact line dynamics also contributes an additional drag term for translations over the interface plane [4] and strongly suppresses rotations about any axis orthogonal to the interface normal [5]. When self-propulsion is added to the mix, as in catalytic Janus microspheres trapped at an interface, capillary forces produce speeds and reorientation times that can be very different from the bulk values [6]. For swimming bacteria we only know that a combination of hydrodynamic and steric interactions can retain cells over the surface of an impenetrable boundary where they trace circular trajectories [7]. For liquid-solid interfaces, these circles are traced counterclockwise [8], when looked at from the solid side, while for liquid-air interfaces the direction is reversed [9,10]. All bacteria display the same swimming pattern that is solely dictated by the boundary conditions imposed by the interface on the fluid [11–14].

Here, we show that, when bacteria colonize a liquid-air interface, a complex interplay between flagellar torque, cap-

illary forces, and hydrodynamic interactions gives rise to four distinct swimming modes. By combining holographic microscopy and theoretical modeling, we demonstrate that each cell selects one of these four swimming modes based on the value of two intrinsic parameters: the orientation of the cell body relatively to the flagellar bundle and the angular stiffness of the bundle.

E. coli cells are often represented by two rigid bodies, a cell body and flagellar bundle, that translate with the same velocity but are free to rotate around a common axis [15]. Freely swimming bacteria are torque free so that an equal and opposite torque is applied by flagellar motors to body and bundle. Both the body and the bundle have time-averaged hydrodynamic resistance tensors with a principal axis parallel to the torque. As a result, internal deformations are only present as small-amplitude oscillations and can be often neglected. In monotrichous bacteria, the presence of the hook, a flexible joint connecting flagella to the cell body, can cause random reorientations through buckling [16,17], while no major role was attributed to the flexibility of flagellar bundles in peritrichous bacteria such as *E. coli*. When a cell breaches a liquid-air interface, the presence of a contact line suppresses out-of-plane motions and only allows body rotations around the surface normal \hat{z} [5]. In this situation, equal and opposite torques result in nonparallel angular velocities and small differences in bundle stiffness and alignment result in very different swimming modes. Three-axis holographic microscopy [10,18–20] provides volumetric reconstructions of the prolate cell body. In adsorbed cells, vertical fluctuations as well as wobbling are strongly suppressed due to contact line pinning and surface tension as shown in Fig. 1. Looking at the trajectories of these interface bound cells, we found a variety of different behaviors. These swimming patterns can be grouped

*roberto.dileonardo@uniroma1.it

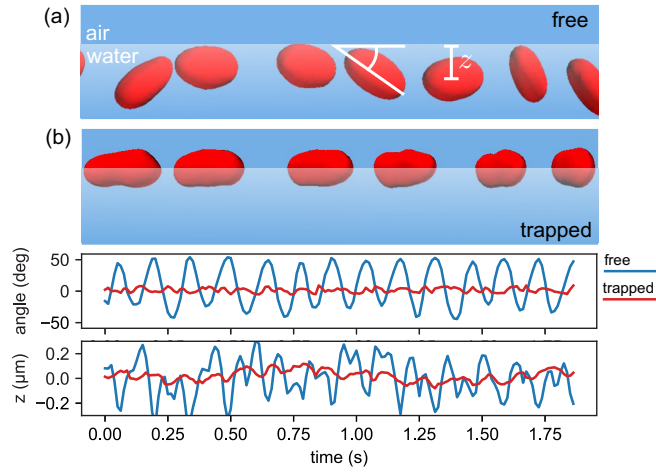


FIG. 1. Side view on volumetric images of (a) a fully wet cell swimming below the water-air interface, and (b) a partially wet cell that is trapped at the interface by capillary forces. The exact location of the interface is not known directly and the one shown in the figure is intended only as a graphical representation.

into four modes that are represented in Figs. 2(a)–2(d). In the top two rows, we have “locked” cells, with the cell body forming a constant angle with the swimming direction while both rotate clockwise (CW) in Fig. 2(a) and counterclockwise (CCW) in Fig. 2(b), when viewed from the air side. The two bottom rows show two examples of “spinning” cells with the body axis always rotating CCW while the body center traces CW [Fig. 2(c)] or CCW [Fig. 2(d)] circles, respectively. Locked cells [Figs. 2(a) and 2(b)] and CW spinning cells [Fig. 2(c)] swim with a stationary dynamics while the trajectories of CCW spinning cells [Fig. 2(d)] are often discontinuous with CCW arcs interrupted by kinks where the cell body rotates faster.

Despite this apparent complexity, the nature and the features of these different swimming modes can be understood by a very simple elasto-hydrodynamic model. We treat the cell body and the bundle as two hydrodynamically uncoupled units connected by a joint at the center of the cell body through which they can exchange a force \mathbf{F} and a torque \mathbf{T} . The cell body linear and angular velocities \mathbf{U} and $\mathbf{\Omega}$ are linearly related to \mathbf{F} and \mathbf{T} by a mobility matrix:

$$\begin{pmatrix} \mathbf{U} \\ \mathbf{\Omega} \end{pmatrix} = \begin{pmatrix} \mathbf{A} & 0 \\ 0 & \mathbf{B} \end{pmatrix} \cdot \begin{pmatrix} \mathbf{F} \\ \mathbf{T} \end{pmatrix}. \quad (1)$$

An equal and opposite force and torque will act on the bundle for which we also must include rototranslational coupling terms:

$$\begin{pmatrix} \mathbf{U} \\ \boldsymbol{\omega} \end{pmatrix} = \begin{pmatrix} \mathbf{a} & \mathbf{c} \\ \mathbf{c}^T & \mathbf{b} \end{pmatrix} \cdot \begin{pmatrix} -\mathbf{F} \\ -\mathbf{T} \end{pmatrix}. \quad (2)$$

All mobility tensors \mathbf{A} , \mathbf{B} , \mathbf{a} , \mathbf{b} , \mathbf{c} are referred to the cell body center. Force and torque in (1) should also include the capillary contributions that behave as reaction forces restricting body translations on the xy plane and rotations to the sole z axis. Instead of explicitly introducing these reaction forces we can use effective mobility matrices [21] that, assuming a

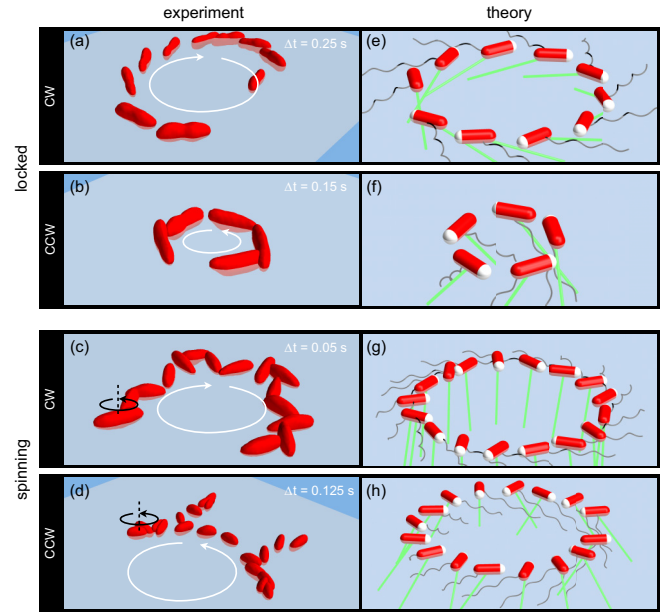


FIG. 2. Swimming modes of interfacial bacteria. The left column shows volumetric reconstructions of *E. coli* cells trapped at a water-air interface. “Locked” cells [(a), (b)] keep a constant angle between the body axis and the velocity vector while for “spinning” cells [(c), (d)] the cell body freely rotates counterclockwise. Both “locked” and “spinning” cells move over circular trajectories that are traced either clockwise [(a), (c)] or counterclockwise [(b), (d)]. The right column shows four sample trajectories generated by direct integration of the equations of motion described in the text. The selected values for parameters θ_0 and k/τ are represented in Fig. 5 over the predicted swimming mode diagram.

spherical cell body, have the following form:

$$\mathbf{A} = A(\hat{\mathbf{x}}\hat{\mathbf{x}} + \hat{\mathbf{y}}\hat{\mathbf{y}}), \quad \mathbf{B} = B\hat{\mathbf{z}}\hat{\mathbf{z}}. \quad (3)$$

We can assume that bundles are fully wetted [21] and are described by constant axisymmetric mobility tensors,

$$\mathbf{a} = a_{\parallel}\hat{\mathbf{I}} + (a_{\perp} + b_{\perp}L^2)(\mathbf{I} - \hat{\mathbf{I}}), \quad (4)$$

$$\mathbf{b} = b_{\parallel}\hat{\mathbf{I}} + b_{\perp}(\mathbf{I} - \hat{\mathbf{I}}), \quad (5)$$

$$\mathbf{c} = -c\hat{\mathbf{I}} - Lb_{\perp}\hat{\mathbf{I}} \times \mathbf{I}, \quad (6)$$

where \mathbf{I} is the identity tensor, $\hat{\mathbf{I}}$ is the bundle axis, $2L$ is the bundle length, while a_{\parallel} , a_{\perp} , b_{\parallel} , b_{\perp} , and c are the mobility components referred to the center of the bundle. Shifting the mobility tensor from the bundle to body center [22] gives the terms $b_{\perp}L^2(\mathbf{I} - \hat{\mathbf{I}})$ in Eq. (4) and $Lb_{\perp}\hat{\mathbf{I}} \times \mathbf{I}$ in Eq. (6). The torque \mathbf{T} has two components: an axial torque transmitted by flagellar motors and an off-axis torque that elastically restores the bundle axis onto an equilibrium direction $\hat{\mathbf{l}}_0$ that is rigidly anchored to the cell body:

$$\mathbf{T} = \tau\hat{\mathbf{I}} - k\hat{\mathbf{I}} \times \hat{\mathbf{l}}_0. \quad (7)$$

Although liquid-air interfaces are all but simple [10] we model our interface as a stress-free boundary. In principle, the presence of an interface will affect all components of the bundle mobility matrices \mathbf{a} , \mathbf{b} , \mathbf{c} but the most important correction

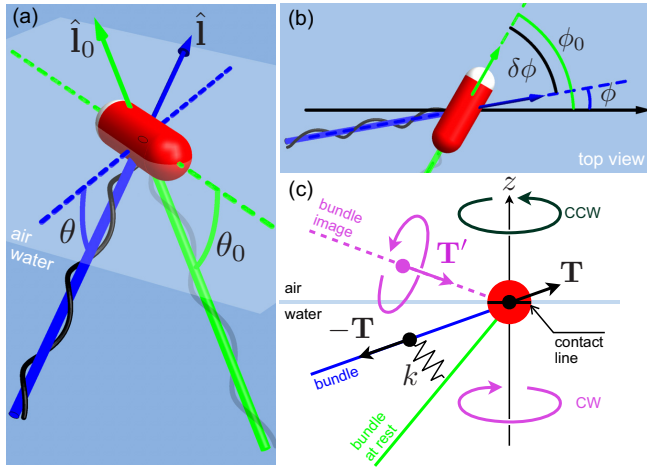


FIG. 3. (a) $\hat{\mathbf{l}}_0$ represents the direction of the bundle at rest and follows rigidly the cell body. $\hat{\mathbf{l}}$ is the actual bundle direction during swimming. The two vectors $\hat{\mathbf{l}}_0$ and $\hat{\mathbf{l}}$ form respectively the angles θ_0 and θ with the interface plane. (b) $\delta\phi$ is the angle between the in-plane projections of $\hat{\mathbf{l}}_0$ and $\hat{\mathbf{l}}$ (dashed lines). (c) \mathbf{T} is the torque exerted by flagellar motors on the cell body and producing CCW rotations around the only available axis for rotations $\hat{\mathbf{z}}$. The hydrodynamic image of the bundle applies a torque \mathbf{T}' on the fluid whose resulting flow advects the real bundle and drives CW rotations.

to bulk mobilities is the appearance of a new coupling term that is responsible for CW swimming at liquid-air interfaces [9]. We find that this term is well estimated by the analytic expression

$$\mathbf{c}' = \frac{(\hat{\mathbf{l}} \times \hat{\mathbf{z}})\hat{\mathbf{l}}}{16\pi\eta L^2 \sin\theta}, \quad (8)$$

obtained by evaluating the flow field produced at the bundle center by a line of torques distributed over the axis of the bundle's hydrodynamic image [9]. The goodness of this approximation is validated by numerical simulations [21]. A generic configuration is described by the vectors $\hat{\mathbf{l}}_0$ and $\hat{\mathbf{l}}$ that rotate with the body and bundle angular velocities $\boldsymbol{\Omega}$ and $\boldsymbol{\omega}$, respectively. In a Cartesian coordinate system with the z axis directed along the interface normal [Fig. 3(c)], $\hat{\mathbf{l}}_0$ and $\hat{\mathbf{l}}$ have coordinates $\hat{\mathbf{l}}_0 = (\cos\theta_0 \cos\phi_0, \cos\theta_0 \sin\phi_0, \sin\theta_0)$ and $\hat{\mathbf{l}} = (\cos\theta \cos\phi, \cos\theta \sin\phi, \sin\theta)$. For our smooth swimming strain, the bundle forms in the bulk and keeps a fixed orientation $\hat{\mathbf{l}}_0$ with respect to the cell body. As the cell body becomes trapped by the interface, the bundle axis $\hat{\mathbf{l}}$ deviates from the equilibrium direction $\hat{\mathbf{l}}_0$ that rotates rigidly with the cell body. Since body rotations are restricted to the z axis, $\hat{\mathbf{l}}_0$ will form a fixed angle θ_0 with the interface plane. For a given configuration specified by θ and $\delta\phi = \phi_0 - \phi$, we can solve the four vector equations (1) and (2) for the four unknown vectors \mathbf{F} , \mathbf{U} , $\boldsymbol{\Omega}$, and $\boldsymbol{\omega}$, once the cell properties θ_0 , k , and τ are specified. We find that the cell body rotates with an angular speed

$$\dot{\phi}_0 = \Omega_z = B\tau \sin\theta - Bk \cos\theta \cos\theta_0 \sin\delta\phi. \quad (9)$$

The azimuthal bundle angle evolves as [23]

$$\dot{\phi} = \omega_z - \tan\theta \omega_x = -\frac{b_\perp \tau}{\alpha} \frac{1}{\sin\theta} + \frac{b_\perp k}{\beta} \frac{\cos\theta_0 \sin\delta\phi}{\cos\theta}, \quad (10)$$

where $\beta = 1 + b_\perp L^2 / (A + a_\perp + b_\perp L^2)$ and $\alpha = 16\pi\eta L(A + a_\perp)$. Equations (9) and (10) imply that, when the bundle is in its rest equilibrium configuration, $\delta\phi = 0$ and the cell body is driven by the motor torque in a CCW (positive z) rotation that is faster the larger is the angle θ . Conversely, the bundle is advected in a CW rotation by the flow produced by image torques that is stronger as θ becomes smaller, and the bundle gets closer to the interface. As the body and the bundle rotate in opposite directions, the angle $\delta\phi = \phi_0 - \phi$ evolves as

$$\frac{\dot{\delta\phi}}{B\tau} = \sin\theta + \frac{b_\perp/B}{\alpha \sin\theta} - \frac{k}{\tau} \left(\cos\theta - \frac{b_\perp/B}{\beta \cos\theta} \right) \cos\theta_0 \sin\delta\phi, \quad (11)$$

where time is normalized in units of $1/B\tau$. As the stiffness k/τ increases, there will be an equilibrium angle $\delta\phi$ for which the cell body and bundle rotations are locked ($\dot{\delta\phi} = 0$) and spin with the same angular speed. The sign of this common speed can be either positive (CCW) or negative (CW) depending on the angle θ only. At the transition between CCW and CW motion, both $\dot{\phi}_0$ and $\dot{\phi}$ will be 0 so that from (9) and (10) we can derive a threshold value for θ :

$$\tan^2\theta^* = \beta/\alpha. \quad (12)$$

For $\theta > \theta^*$ the bundle is sufficiently far from the interface and the z component of flagellar torque on the cell body drives CCW rotations while for $\theta < \theta^*$ the bundle is strongly coupled with the interface causing CW rotations as in free swimming over a liquid interface [9]. This consideration also suggests that for CCW locked cells, the bundle is more vertical and the in-plane component of the thrust is reduced giving rise to circular trajectories with smaller radii, as can be observed comparing Figs. S2(a) and S2(b) in the Supplemental Material [21]. Using numerical values for the mobility matrix [21] we can estimate the magnitude of this threshold angle $\theta^* = 11^\circ$. From (11) we also see that if k/τ is too small we never attain a stationary value for $\delta\phi$ which grows unrestricted. An example of this can be seen in Fig. 2(c) where the cell body constantly spins CCW while the swimming direction, which is approximately parallel to the bundle projection over the interface plane, rotates CW. If our flexible bundle model is correct, the angle $\delta\phi$ between the cell body and the bundle, or equivalently the swimming direction, should grow with a rate that has a sinusoidal dependence on $\delta\phi$. This is clearly visible when we plot the experimental values for $\dot{\delta\phi}$ as a function of $\delta\phi$ as shown in Fig. 4(a). Black circles are obtained by averaging over all spinning CW bacteria after shifting all curves so that $\delta\phi = 0$ corresponds to the equilibrium angle between the body and the bundle. As a further quantitative check we report in Fig. 4(b) the observed time evolution of ϕ_0 and ϕ for a CW spinning cell together with theoretical predictions obtained by numerical integration of (9) and (10) along with the equation governing the evolution of θ [21]. The best fit parameters are all in the expected range: $A = 74 \mu\text{m s}^{-1} \text{pN}^{-1}$, $B = 48 \mu\text{m}^{-1} \text{s}^{-1} \text{pN}^{-1}$, $\tau = 1.25 \text{pN } \mu\text{m}$, $k = 0.56 \text{pN } \mu\text{m}$, $\theta_0 = 60^\circ$, $L = 4.6 \mu\text{m}$. In principle, it could also be possible to have a spinning cell body moving along a CCW trajectory, but most of the times we find trajectories such as the one in Fig. 2(d) that look more like locked CCW trajectories interrupted by transient cell body spins.

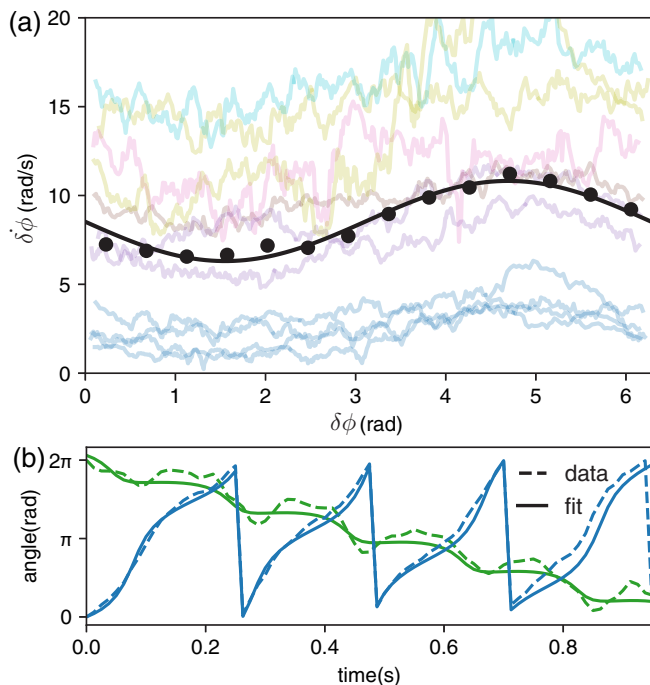


FIG. 4. (a) As predicted by (11), an elastically restored bundle gives a sinusoidal dependence of $\delta\dot{\phi}$ on $\delta\phi$ as observed in all cells (colored lines) and in their average (black circles). The solid black line is the best fit to a sinusoidal curve. (b) Dashed lines represent the experimental angular dynamics of the cell body angle ϕ_0 (teal) and the swimming direction ϕ (green) in a CW spinning state. Solid lines are obtained by numerical integration of Eqs. (9) and (10) and Eq. (S13) in the Supplemental Material [21].

Using numerical estimates for the mobility coefficients [21], we perform numerical integration over a 200×200 grid of θ_0 and k/τ values, and classified solutions as “locked” if $\delta\phi$ reached a stationary value or “spinning” otherwise. We further divide the solutions into CCW or CW according to the sign of (10) evaluated over the numerical trajectory. The resulting map is shown in Fig. 5(a) where we also report, as the surface height, the cell speed U normalized to the bulk value $U_0 = c\tau/(1 + a_{\parallel}/A)$. We see that for stiff bundles ($k/\tau \gg 1$) the transition between CCW and CW occurs at $\theta^* \simeq 11^\circ$. For low k/τ values, we always have CW spinning states while CCW spinning states only exist in a limited range of values. This explains why pure CCW spinning states were not experimentally observed. Different values of body mobility lead to small deformations of the boundaries between swimming modes, but the overall picture remains the same [21]. The distribution of observed swimming modes is represented in Fig. 5(b) where every cell appears at coordinates given by the average values of ϕ_0 and ϕ . We see from the diagram in Fig. 5 that cells have access to all different swimming patterns if k/τ takes values around 1. To provide the order of magnitudes we can first assume that all bending occurs at the hook, whose bending stiffness during swimming was estimated to be $EI \approx 0.1 \text{ pN } \mu\text{m}^2$ for *V. alginolyticus* [16]. Considering a hook length $l \approx 0.1 \mu\text{m}$ we get a torsional spring stiffness $k = EI/l \approx 1 \text{ pN } \mu\text{m}$ which is of the same order of typical estimates for motor torque [19,24–26]. A comparable value

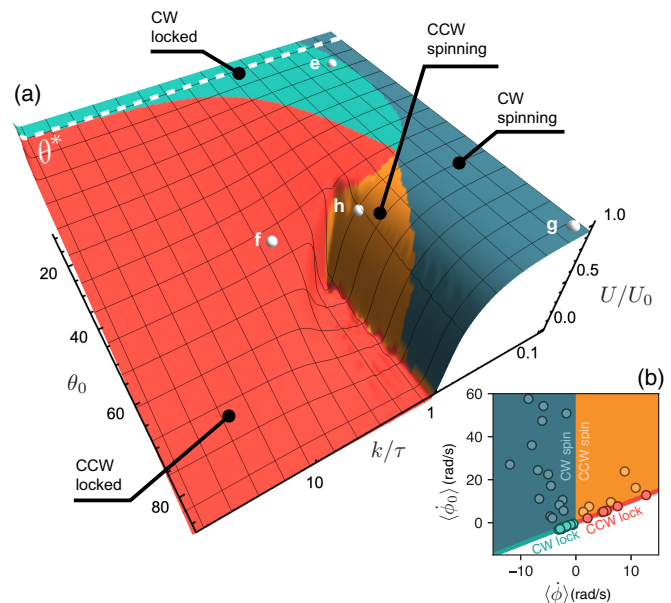


FIG. 5. (a) Theoretical diagram of swimming states generated by varying bundle rest angle θ_0 and normalized stiffness k/τ . The surface height represents the corresponding normalized cell speed. The four white points on the surface represent the parameters used to generate the trajectories in Figs. 2(e)–2(h). (b) Data points falling on the line $\phi_0 = \phi$ represent locked cells, while those in the teal and orange regions are CW and CCW spinning cells, respectively.

is obtained if we assume that the flexibility of the bundle is only due to filament bending. Also in this case we get $k = EI/L \approx 1 \text{ pN } \mu\text{m}$ when we use $EI = 3.5 \text{ pN } \mu\text{m}^2$ [27] for the bending stiffness of flagellar filaments and $2L = 6.9 \mu\text{m}$ for the filament length. We take four representative points on the diagram and directly integrate the equations of motion (1) and (2) using a more realistic, anisotropic form for the mobility matrix $\mathbf{A} = A_{\parallel}\hat{\mathbf{l}}_0\hat{\mathbf{l}}_0 + A_{\perp}(\mathbf{I} - \hat{\mathbf{l}}_0\hat{\mathbf{l}}_0)$ with $A_{\parallel} = 75 \mu\text{m pN}^{-1} \text{ s}^{-1}$ and $A_{\perp} = 61 \mu\text{m pN}^{-1} \text{ s}^{-1}$ as for a prolate spheroid with major and minor axes of 3 and 1 μm , respectively. The corresponding trajectories are shown in the right column of Fig. 2 and are consistent with the swimming modes predicted by the diagram in Fig. 5. By tuning θ_0 and k/τ we can control the geometry of trajectories and select the values that best match experimental trajectories in Figs. 2(a)–2(d). Keeping those values fixed we could match experimental timescales in Fig. 2 by choosing torque values in the range $\tau = 0.6\text{--}2.1 \text{ pN } \mu\text{m}$.

In conclusion, we studied how capillary forces affect swimming in bacteria that are partially wet at a water-air interface. Using a simple analytical model where the cell body is constrained by capillary forces and the flagellar bundle is flexible and hydrodynamically coupled to the interface, we can reproduce the four observed swimming modes by varying two parameters: (i) the equilibrium pitch angle θ_0 of the bundle, and (ii) the normalized stiffness k/τ that, as the cell swims, pulls the bundle back to the equilibrium configuration. Although this simple model can quantitatively reproduce most of the observed trajectories, some features such as the unsteady behavior of CCW spinning cells [Figs. 2(d)–2(h)] remain unexplained. A possible reason could be the intrinsic noise driving real systems across boundaries between

swimming modes. More refined simulation strategies could be used to confirm the validity of our simple picture while experiments with different microswimmers could explore its generality.

This project has received funding from the European Research Council (ERC) under the European Union's Horizon 2020 research and innovation programme (Grant Agreement No. 834615).

-
- [1] L. Vaccari, M. Molaei, T. H. Niepa, D. Lee, R. L. Leheny, and K. J. Stebe, Films of bacteria at interfaces, *Adv. Colloid Interface Sci.* **247**, 561 (2017).
- [2] J. Deng, M. Molaei, N. G. Chisholm, and K. J. Stebe, Motile bacteria at oil-water interfaces: *Pseudomonas aeruginosa*, *Langmuir* **36**, 6888 (2020).
- [3] D. M. Kaz, R. McGorty, M. Mani, M. P. Brenner, and V. N. Manoharan, Physical ageing of the contact line on colloidal particles at liquid interfaces, *Nat. Mater.* **11**, 138 (2012).
- [4] G. Boniello, C. Blanc, D. Fedorenko, M. Medfai, N. B. Mbarek, M. In, M. Gross, A. Stocco, and M. Nobili, Brownian diffusion of a partially wetted colloid, *Nat. Mater.* **14**, 908 (2015).
- [5] A. Stocco, B. Chollet, X. Wang, C. Blanc, and M. Nobili, Rotational diffusion of partially wetted colloids at fluid interfaces, *J. Colloid Interface Sci.* **542**, 363 (2019).
- [6] K. Dietrich, D. Renggli, M. Zanini, G. Volpe, I. Buttinoni, and L. Isa, Two-dimensional nature of the active Brownian motion of catalytic microswimmers at solid and liquid interfaces, *New J. Phys.* **19**, 065008 (2017).
- [7] S. Bianchi, F. Saglimbeni, and R. Di Leonardo, Holographic Imaging Reveals the Mechanism of Wall Entrapment in Swimming Bacteria, *Phys. Rev. X* **7**, 011010 (2017).
- [8] E. Lauga, W. R. DiLuzio, G. M. Whitesides, and H. A. Stone, Swimming in circles: Motion of bacteria near solid boundaries, *Biophys. J.* **90**, 400 (2006).
- [9] R. Di Leonardo, D. Dell'Arciprete, L. Angelani, and V. Iebba, Swimming with an Image, *Phys. Rev. Lett.* **106**, 038101 (2011).
- [10] S. Bianchi, F. Saglimbeni, G. Frangipane, D. Dell'Arciprete, and R. Di Leonardo, 3D dynamics of bacteria wall entrapment at a water-air interface, *Soft Matter* **15**, 3397 (2019).
- [11] L. Lemelle, J.-F. Palierne, E. Chatre, and C. Place, Counter-clockwise circular motion of bacteria swimming at the air-liquid interface, *J. Bacteriol.* **192**, 6307 (2010).
- [12] M. Morse, A. Huang, G. Li, M. R. Maxey, and J. X. Tang, Molecular adsorption steers bacterial swimming at the air/water interface, *Biophys. J.* **105**, 21 (2013).
- [13] L. Lemelle, J.-F. Palierne, E. Chatre, C. Vaillant, and C. Place, Curvature reversal of the circular motion of swimming bacteria probes for slip at solid/liquid interfaces, *Soft Matter* **9**, 9759 (2013).
- [14] J. Hu, A. Wysocki, R. G. Winkler, and G. Gompper, Physical sensing of surface properties by microswimmers – directing bacterial motion via wall slip, *Sci. Rep.* **5**, 9586 (2015).
- [15] J. Higdon, The hydrodynamics of flagellar propulsion: Helical waves, *J. Fluid Mech.* **94**, 331 (1979).
- [16] K. Son, J. S. Guasto, and R. Stocker, Bacteria can exploit a flagellar buckling instability to change direction, *Nat. Phys.* **9**, 494 (2013).
- [17] H. Shum and E. Gaffney, The effects of flagellar hook compliance on motility of monotrichous bacteria: A modeling study, *Phys. Fluids* **24**, 061901 (2012).
- [18] F. Saglimbeni, S. Bianchi, A. Lepore, and R. Di Leonardo, Three-axis digital holographic microscopy for high speed volumetric imaging, *Opt. Express* **22**, 13710 (2014).
- [19] S. Bianchi, F. Saglimbeni, A. Lepore, and R. Di Leonardo, Polar features in the flagellar propulsion of *E. coli* bacteria, *Phys. Rev. E* **91**, 062705 (2015).
- [20] S. Ferretti, S. Bianchi, G. Frangipane, and R. Di Leonardo, A virtual reality interface for the immersive manipulation of live microscopic systems, *Sci. Rep.* **11**, 7610 (2021).
- [21] See Supplemental Material at <http://link.aps.org/supplemental/10.1103/PhysRevResearch.4.L022044> for further details on theoretical modeling, simulations, and supporting figures.
- [22] S. Kim and S. J. Karrila, *Microhydrodynamics: Principles and Selected Applications* (Dover, New York, 2005).
- [23] $\dot{\phi} = \frac{d}{dt} \tan^{-1}(l_y/l_x) = \frac{l_x \dot{l}_y - l_y \dot{l}_x}{l_x^2 + l_y^2} = \frac{(\hat{\mathbf{i}} \times \frac{d\hat{\mathbf{l}}}{dt}) \cdot \hat{\mathbf{z}}}{l_x^2 + l_y^2}$. By substituting the time evolution of the orientation vector $\frac{d\hat{\mathbf{l}}}{dt} = \boldsymbol{\omega} \times \hat{\mathbf{l}}$ one obtains $\dot{\phi} = \frac{(\hat{\mathbf{i}} \times \boldsymbol{\omega}) \cdot \hat{\mathbf{z}}}{l_x^2 + l_y^2}$. Using the triple vector product identity one obtains $\dot{\phi} = \frac{(\hat{\mathbf{i}})(\boldsymbol{\omega} \cdot \hat{\mathbf{z}}) - (\hat{\mathbf{z}})(\hat{\mathbf{i}} \cdot \boldsymbol{\omega})}{l_x^2 + l_y^2}$ that leads to Eq. (10) if the components of $\hat{\mathbf{l}}$ and $\boldsymbol{\omega}$ are substituted.
- [24] S. W. Reid, M. C. Leake, J. H. Chandler, C.-J. Lo, J. P. Armitage, and R. M. Berry, The maximum number of torque-generating units in the flagellar motor of *Escherichia coli* is at least 11, *Proc. Natl. Acad. Sci. USA* **103**, 8066 (2006).
- [25] N. C. Darnton, L. Turner, S. Rojevsky, and H. C. Berg, On torque and tumbling in swimming *Escherichia coli*, *J. Bacteriol.* **189**, 1756 (2007).
- [26] D. Das and E. Lauga, Computing the motor torque of *Escherichia coli*, *Soft Matter* **14**, 5955 (2018).
- [27] N. C. Darnton and H. C. Berg, Force-extension measurements on bacterial flagella: Triggering polymorphic transformations, *Biophys. J.* **92**, 2230 (2007).